The 1st Joint International Conference on Multibody System Dynamics
May 25–27, 2010, Lappeenranta, Finland

Multibody Modelling and Optimization of a Curved Hinge Flexure

Steven E. Boer, Ronald G.K.M. Aarts, Dannis M. Brouwer, J. Ben Jonker

Laboratory of Mechanical Automation and Mechatronics, Faculty of Engineering Technology
University of Twente
P.O. Box 217, 7500 AE Enschede, The Netherlands
e-mail: s.e.boer@utwente.nl

ABSTRACT

A flexure which retains its support stiffness characteristics for large deflections, is optimized with respect to maximum allowable stress, low actuation stiffness and high support stiffnesses. Such an optimization requires an efficient model which accurately describes the stiffness characteristics and stress distribution of flexures. For this purpose a multibody modelling approach based on a non-linear finite element description is investigated and extended to include the computation of the stress distribution in the deformed configuration. It is shown that the accuracy of the maximum occurring stress is comparable with those obtained from a classical non-linear finite element analysis. An optimized shape of the flexure is found and for deflection angles larger than 7.4°, it is preferable over a single leaf-spring flexure.

Keywords: stresses in beams, stress resultants, finite elements, large deflection, leaf-spring.

1 INTRODUCTION

In high precision manipulator mechanisms, flexure elements are often utilized for their deterministic static and dynamic behaviour. A typical example is the leaf-spring flexure, shown in figure 1(a). The leaf-spring has a high support stiffness in x-, z- and r_y-direction, while it has a low actuation stiffness in the r_z-direction. However, with increasing deflection in the r_z-direction, the support stiffnesses rapidly decrease. This results in a deteriorating static and dynamic behaviour of the mechanism, making this flexure element less suited for long stroke applications. Other flexure elements such as the cross-pivot flexure [3], suffer from this same drawback. Recently, a flexure has been introduced that shows promising results in retaining its support stiffness over a large range of deflection [1]. This so called curved hinge flexure (CHF), figure 1(b), consists of two pre-curved stress free leaf-springs. In the deflected state, one of the leaf-springs becomes straight, figure 1(c), providing the support stiffnesses. A drawback of the CHF in its current

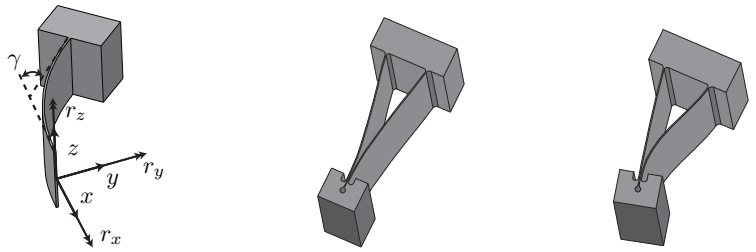

(a) (b) (c)

Figure 1. Leaf-spring flexure (a), curved hinge flexure undeformed state (b) and curved hinge flexure deflected state (c).

design is the occurrence of high stress levels in the deflected state. Smaller stress levels can be obtained with an optimized shape and topology of the flexure, using an adequate optimization criteria: a low actuation stiffness, high support stiffnesses within the working range and a constraint on the allowable stress. For this optimization, an efficient model is required which accurately describes the stiffness characteristics and stress distribution of flexures. The flexible multibody modelling approach implemented in the SPACAR software [4], is based on a non-linear finite element beam description and is well-suited to create the models

for this optimization. In this approach, the geometrically nonlinear relations for the beam element deformations, expressed in terms of the nodal coordinates, play a central role. Its implementation is based on the adoption of an appropriate description of finite rotation kinematics, where properly chosen deformation parameters are defined as generalized strains with energetically dual generalized stress resultants [5]. The approach has already proven to be quite accurate and efficient in predicting stiffness characteristics [7]. However, correctly interpreting the generalized stress resultants of the element in a deformed configuration is not straightforward. In this paper it is shown how the distributed stress resultants, along the elastic line in a deformed configuration, are derived from the generalized stress resultants. The normal and shear stresses in the cross-section can then be computed from the distributed stress resultants. The von Mises criterion is used to determine whether the maximal allowable stress has been exceeded. The computation of the stresses and stiffnesses are used as input in the optimization problem of the CHF.
In section 2 a description is given of the multibody modelling approach of [5], which is extended to acquire the distributed stress resultants and the von Mises stresses. Section 3 gives an overview of the CHF model, the optimization criteria and optimization results. A comparison with a finite element method (FEM) analysis is performed to determine the accuracy of the model. In section 4 the conclusions are presented.

2 THE FINITE BEAM ELEMENT

In this section a description is given of the beam element presented in [5], which is used in the model of the curved hinge flexure (CHF). The concept of the generalized strains and the dual generalized stresses, are explained. Relations are derived for the distributed stress resultants along the elastic line of a deformed beam element, which are used to compute the von Mises stresses in the cross-section of the beam.

2.1 Definition of the coordinate vector and the generalized strains

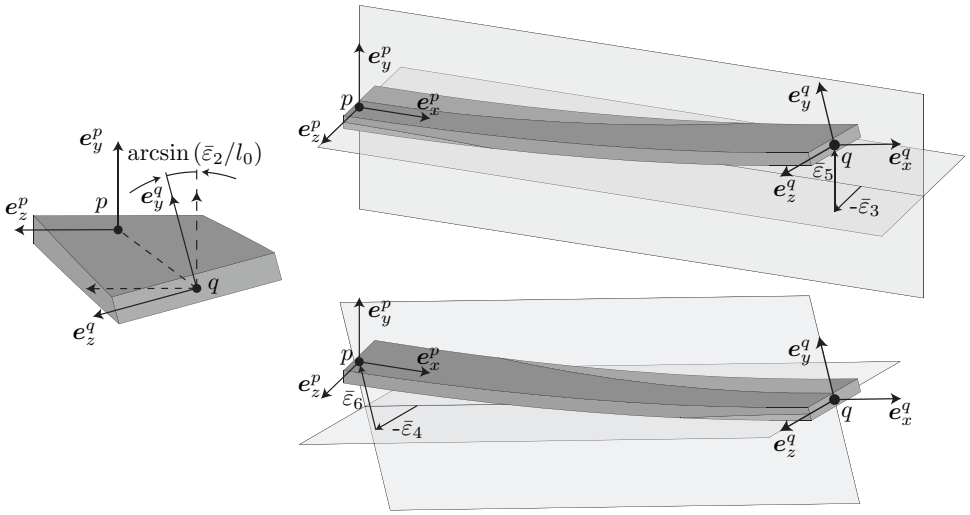

Figure 2. The finite beam element, showing the generalized strains $\bar{\varepsilon}_2$ through $\bar{\varepsilon}_6$. Note that in the left view $\bar{\varepsilon}_{3-6} = 0$ and in the two views on the right $\bar{\varepsilon}_1 = 0$.

In figure 2, different views of the beam element are shown. The configuration of the beam element is defined by position vectors $\boldsymbol{x}_p$ and $\boldsymbol{x}_q$, and the orientation of the orthonormal triads, $\left[\boldsymbol{e}_x^p, \boldsymbol{e}_y^p, \boldsymbol{e}_z^p\right]$ and $\left[\boldsymbol{e}_x^q, \boldsymbol{e}_y^q, \boldsymbol{e}_z^q\right]$, rigidly attached to nodes p and q. The orientation of the triads can be computed by rotation matrices $\boldsymbol{R}^p$ and $\boldsymbol{R}^q$

$$\begin{aligned}\left[\boldsymbol{e}_x^p, \boldsymbol{e}_y^p, \boldsymbol{e}_z^p\right] &= \boldsymbol{R}^p \left[\boldsymbol{e}_X, \boldsymbol{e}_Y, \boldsymbol{e}_Z\right], \\ \left[\boldsymbol{e}_x^q, \boldsymbol{e}_y^q, \boldsymbol{e}_z^q\right] &= \boldsymbol{R}^q \left[\boldsymbol{e}_X, \boldsymbol{e}_Y, \boldsymbol{e}_Z\right],\end{aligned} \tag{1}$$

where $\boldsymbol{e}_X$, $\boldsymbol{e}_Y$ and $\boldsymbol{e}_Z$ are the unit vectors in the global coordinate system. The rotation matrices $\boldsymbol{R}^p$ and $\boldsymbol{R}^q$ can be parametrized in several ways such as Euler parameters, modified Euler angles, Rodriques parameters and the Cartesian rotation vector. Here the Cartesian rotation vector is used to parametrize the

rotation matrix, because it provides a natural way of representing the rotation axis and the rotation around this axis. The rotation matrix can be written in terms of the Cartesian rotation vector, as [2]

$$\boldsymbol{R} = \boldsymbol{I}\cos\psi + \frac{\sin\psi}{\psi}\tilde{\boldsymbol{\psi}} + \frac{1-\cos\psi}{\psi^2}\boldsymbol{\psi}\boldsymbol{\psi}^{\mathrm{T}} \quad \text{with} \quad \psi = \|\boldsymbol{\psi}\|\,, \tag{2}$$

and

$$\boldsymbol{\psi} = \begin{bmatrix} \psi_x \\ \psi_y \\ \psi_z \end{bmatrix}, \quad \tilde{\boldsymbol{\psi}} = \begin{bmatrix} 0 & -\psi_z & \psi_y \\ \psi_z & 0 & -\psi_x \\ -\psi_y & \psi_x & 0 \end{bmatrix}, \tag{3}$$

where $\boldsymbol{\psi}$ is the Cartesian rotation vector and ψ the angle of rotation. Together with the three position coordinates, a total of six coordinates are needed to define the location and orientation of a node. For the whole element, these parameters can be combined in the nodal coordinate vector $\boldsymbol{x}$:

$$\boldsymbol{x} = \left[\boldsymbol{x}^{p\mathrm{T}}, \boldsymbol{\psi}^{p\mathrm{T}}, \boldsymbol{x}^{q\mathrm{T}}, \boldsymbol{\psi}^{q\mathrm{T}}\right]^{\mathrm{T}}, \tag{4}$$

where $\boldsymbol{x}^p$ and $\boldsymbol{x}^q$ are the position vectors and $\boldsymbol{\psi}^p$ and $\boldsymbol{\psi}^q$ are the Cartesian rotation vectors of node p and q respectively. Since the beam element has twelve independent nodal coordinates and six rigid body modes, six independent deformation modes, specified by a set of generalized strains $\bar{\boldsymbol{\varepsilon}}$ [5], can be expressed as analytical functions of the nodal coordinate vector $\boldsymbol{x}$ and the original length l_0,

$$\bar{\boldsymbol{\varepsilon}} = \bar{\boldsymbol{\mathcal{D}}}\left(\boldsymbol{x}\right), \tag{5}$$

where

$$\begin{aligned}
\bar{\varepsilon}_1 &= l - l_0, \\
\bar{\varepsilon}_2 &= l_0\left(\boldsymbol{e}_z^p \cdot \boldsymbol{e}_y^q - \boldsymbol{e}_y^p \cdot \boldsymbol{e}_z^q\right)/2, \\
\bar{\varepsilon}_3 &= -l_0 \boldsymbol{e}_l \cdot \boldsymbol{e}_z^p, \\
\bar{\varepsilon}_4 &= l_0 \boldsymbol{e}_l \cdot \boldsymbol{e}_z^q, \\
\bar{\varepsilon}_5 &= l_0 \boldsymbol{e}_l \cdot \boldsymbol{e}_y^p, \\
\bar{\varepsilon}_6 &= -l_0 \boldsymbol{e}_l \cdot \boldsymbol{e}_y^q,
\end{aligned} \tag{6}$$

$$\text{with} \quad l = \|\boldsymbol{x}^q - \boldsymbol{x}^p\| \quad \text{and} \quad \boldsymbol{e}_l = \left(\boldsymbol{x}^q - \boldsymbol{x}^p\right)/l.$$

The first generalized strain, $\bar{\varepsilon}_1$, describes the elongation of the beam, the second one, $\bar{\varepsilon}_2$, describes the torsion and the remaining four are the bending strains. The generalized strains $\bar{\varepsilon}_{2-6}$ are visualized in figure 2. To better describe the influence of loading of the element on its stiffness properties, the generalized strains are modified as [6] [7]:

$$\boldsymbol{\varepsilon} = \boldsymbol{\mathcal{D}}\left(\boldsymbol{x}\right). \tag{7}$$

where,

$$\begin{aligned}
\varepsilon_1 &= \bar{\varepsilon}_1 + \left(2\bar{\varepsilon}_3^2 + \bar{\varepsilon}_3\bar{\varepsilon}_4 + 2\bar{\varepsilon}_4^2 + 2\bar{\varepsilon}_5^2 + \bar{\varepsilon}_5\bar{\varepsilon}_6 + 2\bar{\varepsilon}_6^2\right)/\left(30 l_0\right) + c_t\bar{\varepsilon}_2^2/\left(2l_0^3\right), \\
\varepsilon_2 &= \bar{\varepsilon}_2 + \left(-\bar{\varepsilon}_3\bar{\varepsilon}_6 + \bar{\varepsilon}_4\bar{\varepsilon}_5\right)/l_0, \\
\varepsilon_3 &= \bar{\varepsilon}_3 + \bar{\varepsilon}_2\left(\bar{\varepsilon}_5 + \bar{\varepsilon}_6\right)/\left(6l_0\right), \\
\varepsilon_4 &= \bar{\varepsilon}_4 - \bar{\varepsilon}_2\left(\bar{\varepsilon}_5 + \bar{\varepsilon}_6\right)/\left(6l_0\right), \\
\varepsilon_5 &= \bar{\varepsilon}_5 - \bar{\varepsilon}_2\left(\bar{\varepsilon}_3 + \bar{\varepsilon}_4\right)/\left(6l_0\right), \\
\varepsilon_6 &= \bar{\varepsilon}_6 + \bar{\varepsilon}_2\left(\bar{\varepsilon}_3 + \bar{\varepsilon}_4\right)/\left(6l_0\right).
\end{aligned} \tag{8}$$

These are the second order generalized strain definitions. The additional terms in ε_1 take into account extra elongation due to bending and torsion. For ε_2, the additional terms are due to extra torsion caused by bending and for ε_3 through ε_6 they represent additional bending caused by torsional deformation of the beam.

2.2 Nodal forces and moments

Let us consider the equilibrium force system given by the nodal forces, $\boldsymbol{F}^p$ and $\boldsymbol{F}^q$, and nodal moments, $\boldsymbol{T}^p$ and $\boldsymbol{T}^q$, represented in a vector of element nodal forces

$$\boldsymbol{f} = \left[\boldsymbol{F}^{p\mathrm{T}}, \boldsymbol{T}^{p\mathrm{T}}, \boldsymbol{F}^{q\mathrm{T}}, \boldsymbol{T}^{q\mathrm{T}}\right]^{\mathrm{T}}, \tag{9}$$

then the energetically dual virtual nodal variations are the virtual nodal displacements, $\delta \boldsymbol{x}^p$ and $\delta \boldsymbol{x}^q$, and the virtual rotations, $\delta \boldsymbol{\varphi}^p$ and $\delta \boldsymbol{\varphi}^p$, given by

$$\delta \boldsymbol{u} = \left[\delta \boldsymbol{x}^{p\mathrm{T}}, \delta \boldsymbol{\varphi}^{p\mathrm{T}}, \delta \boldsymbol{x}^{q\mathrm{T}}, \delta \boldsymbol{\varphi}^{q\mathrm{T}}\right]^{\mathrm{T}}. \tag{10}$$

The virtual rotations $\delta \boldsymbol{\varphi}$ are infinitesimal rotations around the global coordinate axes and are related to virtual variations $\delta \boldsymbol{\psi}$ by

$$\delta \boldsymbol{\varphi} = \left(\mathbf{T}\left(\boldsymbol{\psi}\right)\right)^{\mathrm{T}} \delta \boldsymbol{\psi} = \left(\left(\frac{\sin \|\boldsymbol{\psi}\|}{\|\boldsymbol{\psi}\|}\right) \boldsymbol{I} + \left(\frac{1-\cos \|\boldsymbol{\psi}\|}{\|\boldsymbol{\psi}\|^2}\right) \tilde{\boldsymbol{\psi}} + \left(\frac{\|\boldsymbol{\psi}\| - \sin \|\boldsymbol{\psi}\|}{\|\boldsymbol{\psi}\|^3}\right) \boldsymbol{\psi}\boldsymbol{\psi}^{\mathrm{T}}\right) \delta \boldsymbol{\psi}, \tag{11}$$

where $\mathbf{T}$ is the so-called tangent operator [2]. Using equation (11), the relation between $\delta \boldsymbol{u}$ and the virtual variations of the nodal coordinate vector $\delta \boldsymbol{x}$ of equation (4), is given by a block diagonal matrix $\boldsymbol{A}$:

$$\delta \boldsymbol{x} = \boldsymbol{A} \delta \boldsymbol{u} = \operatorname{diag}\left[\boldsymbol{I}; \left(\mathbf{T}\left(\boldsymbol{\psi}^p\right)\right)^{-\mathrm{T}}; \boldsymbol{I}; \left(\mathbf{T}\left(\boldsymbol{\psi}^q\right)\right)^{-\mathrm{T}}\right] \delta \boldsymbol{u}. \tag{12}$$

According to the principle of virtual work, the element will be in a state of equilibrium if

$$\boldsymbol{f}^{\mathrm{T}} \delta \boldsymbol{u} = \boldsymbol{\sigma}^{\mathrm{T}} \delta \boldsymbol{\varepsilon}, \tag{13}$$

holds for all $\delta \boldsymbol{\varepsilon}$ compatible with

$$\delta \boldsymbol{\varepsilon} = \frac{\partial \boldsymbol{\mathcal{D}}\left(\boldsymbol{x}\right)}{\partial \boldsymbol{x}} \delta \boldsymbol{x}. \tag{14}$$

Here the components of the vector $\boldsymbol{\sigma}$ are defined to be dual to the generalized strains and are called the generalized stress resultants. With equation (12) we obtain

$$\boldsymbol{f}^{\mathrm{T}} \delta \boldsymbol{u} = \boldsymbol{\sigma}^{\mathrm{T}} \boldsymbol{D} \delta \boldsymbol{u}, \quad \text{with} \quad \boldsymbol{D} = \frac{\partial \boldsymbol{\varepsilon}}{\partial \boldsymbol{u}} = \frac{\partial \boldsymbol{\mathcal{D}}\left(\boldsymbol{x}\right)}{\partial \boldsymbol{x}} \boldsymbol{A}. \tag{15}$$

This yields the equilibrium equations of the beam element

$$\boldsymbol{f} = \boldsymbol{D}^{\mathrm{T}} \boldsymbol{\sigma}, \tag{16}$$

where the matrix $\boldsymbol{D}$ is the Jacobian matrix which can be found directly without making use of the transformation matrix $\boldsymbol{A}$.

2.2.1 The Jacobian matrix

Consider a vector $\boldsymbol{e}$ undergoing an infinitesimal virtual rotation $\delta \boldsymbol{\varphi}$ around the global axes, resulting in

$$\boldsymbol{e}' = \boldsymbol{R}\boldsymbol{e} = \left(\boldsymbol{I} + \delta \tilde{\boldsymbol{\varphi}}\right) \boldsymbol{e}, \tag{17}$$

where the tilde denotes a skew symmetric matrix. Defining the virtual change between $\boldsymbol{e}'$ and $\boldsymbol{e}$ to be

$$\delta \boldsymbol{e} \equiv \boldsymbol{e}' - \boldsymbol{e} = \delta \tilde{\boldsymbol{\varphi}} \boldsymbol{e} = \delta \boldsymbol{\varphi} \times \boldsymbol{e}, \tag{18}$$

then by taking $\boldsymbol{e}$ to be the columns of the rotation matrices of equation (1), the following expressions can be derived:

$$\delta \boldsymbol{e}_x^p = \delta \boldsymbol{\varphi}^p \times \boldsymbol{e}_x^p, \quad \delta \boldsymbol{e}_y^p = \delta \boldsymbol{\varphi}^p \times \boldsymbol{e}_y^p, \quad \delta \boldsymbol{e}_z^p = \delta \boldsymbol{\varphi}^p \times \boldsymbol{e}_x^p, \tag{19}$$

$$\delta \boldsymbol{e}_x^q = \delta \boldsymbol{\varphi}^q \times \boldsymbol{e}_x^q, \quad \delta \boldsymbol{e}_y^q = \delta \boldsymbol{\varphi}^q \times \boldsymbol{e}_y^q, \quad \delta \boldsymbol{e}_z^q = \delta \boldsymbol{\varphi}^q \times \boldsymbol{e}_x^q. \tag{20}$$

With these relations the Jacobian matrix from equation (16) can be found directly. If the second order generalized strain expressions are not considered, then by taking the derivatives of the expressions in equation (6) with respect to $\boldsymbol{u}$ we obtain [5]

$$\bar{\boldsymbol{D}} = \frac{\partial \bar{\boldsymbol{\varepsilon}}}{\partial \boldsymbol{u}} = \begin{bmatrix}
-\boldsymbol{e}_l^{\mathrm{T}} & \mathbf{0}^{\mathrm{T}} & \boldsymbol{e}_l^{\mathrm{T}} & \mathbf{0}^{\mathrm{T}} \\
\mathbf{0}^{\mathrm{T}} & \frac{l_0}{2}\left[\tilde{\boldsymbol{e}}_z^p \boldsymbol{e}_y^q - \tilde{\boldsymbol{e}}_y^p \boldsymbol{e}_z^q\right]^{\mathrm{T}} & \mathbf{0}^{\mathrm{T}} & \frac{l_0}{2}\left[\tilde{\boldsymbol{e}}_y^q \boldsymbol{e}_z^p - \tilde{\boldsymbol{e}}_z^q \boldsymbol{e}_y^p\right]^{\mathrm{T}} \\
\frac{l_0}{l}\left[\boldsymbol{e}_z^p - \left(\boldsymbol{e}_l^{\mathrm{T}} \boldsymbol{e}_z^p\right) \boldsymbol{e}_l\right]^{\mathrm{T}} & -l_0 \left(\boldsymbol{e}_z^p \times \boldsymbol{e}_l\right)^{\mathrm{T}} & -\frac{l_0}{l}\left[\boldsymbol{e}_z^p - \left(\boldsymbol{e}_l^{\mathrm{T}} \boldsymbol{e}_z^p\right) \boldsymbol{e}_l\right]^{\mathrm{T}} & \mathbf{0}^{\mathrm{T}} \\
-\frac{l_0}{l}\left[\boldsymbol{e}_z^q - \left(\boldsymbol{e}_l^{\mathrm{T}} \boldsymbol{e}_z^q\right) \boldsymbol{e}_l\right]^{\mathrm{T}} & \mathbf{0}^{\mathrm{T}} & \frac{l_0}{l}\left[\boldsymbol{e}_z^q - \left(\boldsymbol{e}_l^{\mathrm{T}} \boldsymbol{e}_z^q\right) \boldsymbol{e}_l\right]^{\mathrm{T}} & l_0 \left(\boldsymbol{e}_z^q \times \boldsymbol{e}_l\right)^{\mathrm{T}} \\
-\frac{l_0}{l}\left[\boldsymbol{e}_y^p - \left(\boldsymbol{e}_l^{\mathrm{T}} \boldsymbol{e}_y^p\right) \boldsymbol{e}_l\right]^{\mathrm{T}} & l_0 \left(\boldsymbol{e}_y^p \times \boldsymbol{e}_l\right)^{\mathrm{T}} & \frac{l_0}{l}\left[\boldsymbol{e}_y^p - \left(\boldsymbol{e}_l^{\mathrm{T}} \boldsymbol{e}_y^p\right) \boldsymbol{e}_l\right]^{\mathrm{T}} & \mathbf{0}^{\mathrm{T}} \\
\frac{l_0}{l}\left[\boldsymbol{e}_y^q - \left(\boldsymbol{e}_l^{\mathrm{T}} \boldsymbol{e}_y^q\right) \boldsymbol{e}_l\right]^{\mathrm{T}} & \mathbf{0}^{\mathrm{T}} & -\frac{l_0}{l}\left[\boldsymbol{e}_y^q - \left(\boldsymbol{e}_l^{\mathrm{T}} \boldsymbol{e}_y^q\right) \boldsymbol{e}_l\right]^{\mathrm{T}} & -l_0 \left(\boldsymbol{e}_y^q \times \boldsymbol{e}_l\right)^{\mathrm{T}}
\end{bmatrix}. \tag{21}$$

When the second order generalized strain expressions are taking into account, the derivatives of equation (8) need to be computed with respect to $\boldsymbol{u}$. For ε_1 this is

$$\frac{\partial \varepsilon_1}{\partial \boldsymbol{u}} = \frac{\partial \bar{\varepsilon}_1}{\partial \boldsymbol{u}} + \frac{c_t \bar{\varepsilon}_2}{l_0^3}\frac{\partial \bar{\varepsilon}_2}{\partial \boldsymbol{u}} + \frac{4\bar{\varepsilon}_3 + \bar{\varepsilon}_4}{30 l_0}\frac{\partial \bar{\varepsilon}_3}{\partial \boldsymbol{u}} + \frac{4\bar{\varepsilon}_4 + \bar{\varepsilon}_3}{30 l_0}\frac{\partial \bar{\varepsilon}_4}{\partial \boldsymbol{u}} + \frac{4\bar{\varepsilon}_5 + \bar{\varepsilon}_6}{30 l_0}\frac{\partial \bar{\varepsilon}_5}{\partial \boldsymbol{u}} + \frac{4\bar{\varepsilon}_6 + \bar{\varepsilon}_5}{30 l_0}\frac{\partial \bar{\varepsilon}_6}{\partial \boldsymbol{u}}. \quad (22)$$

Similarly, the derivatives for ε_{2-6} can be computed, where the resulting Jacobian matrix can be written as a matrix multiplication of equation (21),

$$\boldsymbol{D} = \boldsymbol{E}\,\bar{\boldsymbol{D}}, \quad \text{with} \quad \boldsymbol{E} = \begin{bmatrix} 1 & \frac{c_t\bar{\varepsilon}_2}{l_0^3} & \frac{4\bar{\varepsilon}_3+\bar{\varepsilon}_4}{30l_0} & \frac{4\bar{\varepsilon}_4+\bar{\varepsilon}_3}{30l_0} & \frac{4\bar{\varepsilon}_5+\bar{\varepsilon}_6}{30l_0} & \frac{4\bar{\varepsilon}_6+\bar{\varepsilon}_5}{30l_0} \\ 0 & 1 & -\frac{\bar{\varepsilon}_6}{l_0} & \frac{\bar{\varepsilon}_5}{l_0} & \frac{\bar{\varepsilon}_4}{l_0} & -\frac{\bar{\varepsilon}_3}{l_0} \\ 0 & \frac{\bar{\varepsilon}_5+\bar{\varepsilon}_6}{6l_0} & 1 & 0 & \frac{\bar{\varepsilon}_2}{6l_0} & \frac{\bar{\varepsilon}_2}{6l_0} \\ 0 & -\frac{\bar{\varepsilon}_5+\bar{\varepsilon}_6}{6l_0} & 0 & 1 & -\frac{\bar{\varepsilon}_2}{6l_0} & -\frac{\bar{\varepsilon}_2}{6l_0} \\ 0 & -\frac{\bar{\varepsilon}_3+\bar{\varepsilon}_4}{6l_0} & -\frac{\bar{\varepsilon}_2}{6l_0} & -\frac{\bar{\varepsilon}_2}{6l_0} & 1 & 0 \\ 0 & \frac{\bar{\varepsilon}_3+\bar{\varepsilon}_4}{6l_0} & \frac{\bar{\varepsilon}_2}{6l_0} & \frac{\bar{\varepsilon}_2}{6l_0} & 0 & 1 \end{bmatrix}. \quad (23)$$

2.2.2 The distributed stress resultants

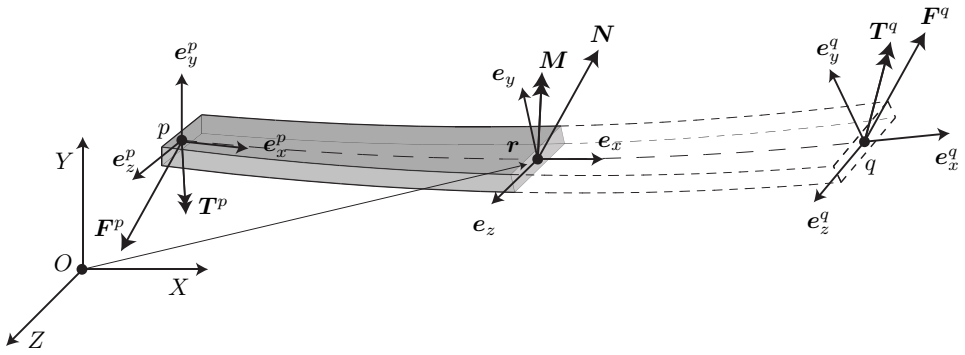

Figure 3. The finite beam element, showing the nodal forces, $\boldsymbol{F}^p$ and $\boldsymbol{F}^q$, nodal moments, $\boldsymbol{T}^p$ and $\boldsymbol{T}^q$, and the stress resultants, $\boldsymbol{N}$ and $\boldsymbol{M}$ in the global coordinate system.

The configuration of the beam element is described by the position vector $\boldsymbol{r}$ on the elastic line from the inertial origin, and a body-fixed frame $[\boldsymbol{e}_x, \boldsymbol{e}_y, \boldsymbol{e}_z]$ representing the orientation of the cross-section with respect to the inertial frame. It is noted that the beam cross-section is allowed to rotate such that it is not necessarily perpendicular to the neutral axis, in order to model transverse shear deformations. The orientation of the body-fixed reference frame with respect to the inertial frame is expressed as

$$[\boldsymbol{e}_x, \boldsymbol{e}_y, \boldsymbol{e}_z] = \boldsymbol{R}(\xi_x)\,[\boldsymbol{e}_X, \boldsymbol{e}_Y, \boldsymbol{e}_Z], \quad \text{with} \quad \xi_x \in [0,1], \quad (24)$$

where $\boldsymbol{R}$ is a rotation matrix with $\boldsymbol{R}(0) = \boldsymbol{R}^p$ and $\boldsymbol{R}(1) = \boldsymbol{R}^q$. The components of the matrix $\boldsymbol{R}$ are computed from the beam shape functions of the Timoshenko beam model presented in [5].
For the case of small element deflections, the distributed stress resultants $\boldsymbol{N}$ and $\boldsymbol{M}$ for the left handed side of the beam shown in figure 3, are expressed as

$$\begin{aligned} \boldsymbol{N} &= \boldsymbol{F}^q = -\boldsymbol{F}^p, \\ \boldsymbol{M}(\xi_x) &= \boldsymbol{T}^p(\xi_x - 1) + \boldsymbol{T}^q\xi_x, \quad \xi_x \in [0,1], \end{aligned} \quad (25)$$

where $\boldsymbol{F}^p$ and $\boldsymbol{F}^q$ are the element nodal forces and $\boldsymbol{T}^p$ and $\boldsymbol{T}^q$ are the element nodal moments, respectively defined by equation (16). The nodal forces and moments depend on the generalized stress resultants $\boldsymbol{\sigma}$,

which are computed from a kinetostatic analysis on system level. For the special case of zero deformation, equation (25) simplifies to

$$\boldsymbol{N} = \begin{bmatrix} N_x \\ N_y \\ N_z \end{bmatrix} = \begin{bmatrix} \sigma_1 \\ \sigma_5 - \sigma_6 \\ \sigma_4 - \sigma_3 \end{bmatrix}, \quad \boldsymbol{M}(\xi_x) = \begin{bmatrix} M_x \\ M_y(\xi_x) \\ M_z(\xi_x) \end{bmatrix} = \begin{bmatrix} l_0\sigma_2 \\ l_0(1-\xi_x)\sigma_3 + l_0\xi_x\sigma_4 \\ l_0(1-\xi_x)\sigma_5 + l_0\xi_x\sigma_6 \end{bmatrix}, \tag{26}$$

where σ_{1-6} are the six components of $\boldsymbol{\sigma}$ dual to $\boldsymbol{\varepsilon}$.
The distributed stress resultants from equation (25) can be transformed to the local coordinate system using equation (24),

$$\begin{aligned} \boldsymbol{N}'(\xi_x) &= (\boldsymbol{R}(\xi_x))^{\mathrm{T}} \boldsymbol{N}, \\ \boldsymbol{M}'(\xi_x) &= (\boldsymbol{R}(\xi_x))^{\mathrm{T}} \boldsymbol{M}(\xi_x), \end{aligned} \tag{27}$$

where $\boldsymbol{N}'$ and $\boldsymbol{M}'$ are the stress resultants in the local axes and their individual components are

$$\boldsymbol{N}'(\xi_x) = \left[N'_x(\xi_x), N'_y(\xi_x), N'_z(\xi_x)\right]^{\mathrm{T}} \quad \text{and} \quad \boldsymbol{M}'(\xi_x) = \left[M'_x(\xi_x), M'_y(\xi_x), M'_z(\xi_x)\right]^{\mathrm{T}}, \tag{28}$$

where N'_x, N'_y and N'_z are the normal and the shear forces and M'_x, M'_y and M'_z are the torsion and bending moments acting in the local coordinate system in the deformed configuration.

2.3 Stress distribution in a rectangular cross-section

The stresses in the cross-section, in the sense of normal and shear stresses, can directly be obtained from the stress resultants of equation (27). The normal and shear stresses for a beam element can be written as

$$\begin{aligned} \sigma_x(\xi_x,\xi_y,\xi_z) &= \sigma_x^{N_x}(\xi_x) + \sigma_x^{M_y}(\xi_x,\xi_z) + \sigma_x^{M_z}(\xi_x,\xi_y), \\ \tau_{xy}(\xi_x,\xi_y,\xi_z) &= \tau_{xy}^{N_y}(\xi_x,\xi_y) + \tau_{xy}^{M_x}(\xi_x,\xi_y,\xi_z), \qquad \text{with} \quad \xi_y \in [-1,1], \quad \xi_z \in [-1,1], \\ \tau_{xz}(\xi_x,\xi_y,\xi_z) &= \tau_{xz}^{N_z}(\xi_x,\xi_z) + \tau_{xz}^{M_x}(\xi_x,\xi_y,\xi_z), \end{aligned} \tag{29}$$

where $\sigma_x^{N_x}$, $\sigma_x^{M_y}$ and $\sigma_x^{M_y}$ are normal stresses caused by the normal force and the bending moments around the local y and z-axis, $\tau_{xy}^{N_y}$, $\tau_{xz}^{N_z}$ are shear stresses caused by the shear forces acting in the local y and z-direction, and $\tau_{xy}^{M_x}$ and $\tau_{xz}^{M_x}$ are shear stresses caused by torsion. Expressions for the normal stresses in case of a rectangular cross-section are

$$\sigma_x^{N_x}(\xi_x) = \frac{N'_x(\xi_x)}{w\,h}, \quad \sigma_x^{M_y}(\xi_x,\xi_z) = \frac{M'_y(\xi_x)\,\xi_z w}{2I_y} \quad \text{and} \quad \sigma_x^{M_z}(\xi_x,\xi_y) = -\frac{M'_z(\xi_x)\,\xi_y h}{2I_z}, \tag{30}$$

where h and w are the height and the width of the cross-section, I_y and I_z are the area moments of inertia for a rectangular cross-section about the local y and z-axis. Expressions for the shear stresses caused by the shear forces are

$$\tau_{xy}^{N_y}(\xi_x,\xi_y) = \frac{3N'_y(\xi_x)\left(1-\xi_y^2\right)}{2\,w\,h} \quad \text{and} \quad \tau_{xz}^{N_z}(\xi_x,\xi_z) = \frac{3N'_z(\xi_x)\left(1-\xi_z^2\right)}{2\,w\,h}. \tag{31}$$

For the torsion shear stresses, Prandtl's membrane analogy should be used, resulting in [8]

$$\begin{aligned} \tau_{xy}^{M_x}(\xi_x,\xi_y,\xi_z) &= \frac{8M'_x(\xi_x)\,w}{\pi^2 I_t} \sum_{n=1,3,5\ldots}^{\infty} \frac{1}{n^2}(-1)^{(n-1)/2}\left(1 - \frac{\cosh\frac{n\pi\xi_y h}{2w}}{\cosh\frac{n\pi h}{2w}}\right)\sin\frac{n\pi\xi_z}{2}, \\ \tau_{xz}^{M_x}(\xi_x,\xi_y,\xi_z) &= -\frac{8M'_x(\xi_x)\,w}{\pi^2 I_t} \sum_{n=1,3,5\ldots}^{\infty} \frac{1}{n^2}(-1)^{(n-1)/2}\left(\frac{\sinh\frac{n\pi\xi_y h}{2w}}{\cosh\frac{n\pi h}{2w}}\right)\cos\frac{n\pi\xi_z}{2}, \end{aligned} \tag{32}$$

where I_t is the Saint-Venant torsion constant.
From the stresses of equation (29), an equivalent stress in the sense of the von Mises criterion, can be computed

$$\sigma_{eq}(\xi_x,\xi_y,\xi_z) = \sqrt{\left(\sigma_x(\xi_x,\xi_y,\xi_z)\right)^2 + 3\left(\tau_{xy}(\xi_x,\xi_y,\xi_z)\right)^2 + 3\left(\tau_{xz}(\xi_x,\xi_y,\xi_z)\right)^2}, \tag{33}$$

which gives the von Mises stresses as a function of the position along the elastic line and in the cross-section. It can be used to check whether the maximal allowable stress in the beam element is not exceeded.

3 MODELLING AND OPTIMIZATION OF THE CURVED HINGE FLEXURE

In this section a parameterized model of the CHF is presented. For the optimization of the CHF, adequate optimization criteria are derived. The final results of the optimization are compared with a FEM analysis to illustrate the quality of the model.

3.1 Curved hinge flexure model

The model of the CHF is defined by a number of fixed parameters, such as material properties, and variable parameters that can be adjusted for optimization purposes. These parameters are e.g. leaf-spring dimensions and the pre-curved shape of the individual leaf-spring flexures. The fixed and variable parameters are visualized in figure 4 and will be explained next. The CHF model consists of twelve flexible pre-curved

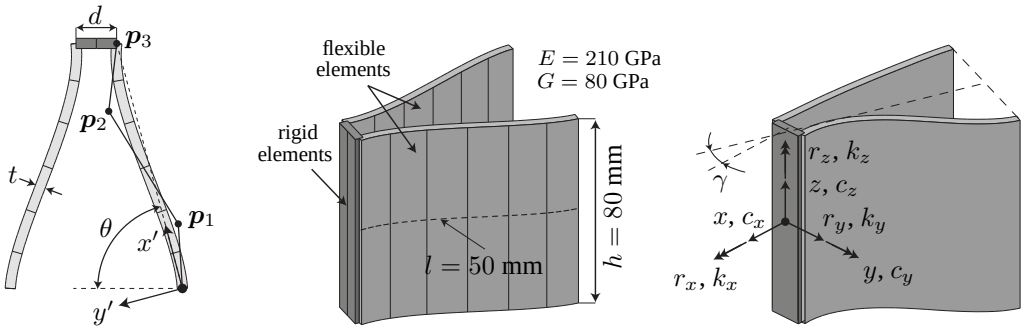

(a) Variable parameters (b) Fixed parameters (c) Coordinate system

Figure 4. Curved hinge flexure model. Model parameters (a)(b) and coordinate system in deflected state (c).

beam elements and two rigid beam elements. It is symmetric in the undeformed configuration. The pre-curved shape is defined by a third order Bézier curve, making it possible to describe a wide variety of curves using only a few parameters. The fixed properties of the beam elements are the Young's modulus, E, the shear modulus, G, the height of the CHF, h, and the length of the Bézier curve, l. The variable parameters are the thickness of the leaf-spring flexures, t, the distance between the leaf-spring flexures, d, and the parameters that define the Bézier curve: the position of the control points $\boldsymbol{p}_1$ and $\boldsymbol{p}_2$ in the local coordinate system $x'y'$, and the inclination angle θ. The position of control point $\boldsymbol{p}_3$ is not an independent model parameter as its position on the local x'-axis, is determined by the fixed length l.
The coordinate system shown in figure 4(c) is rigidly attached to the CHF. At this position, the translational stiffnesses, c_x, c_y and c_z, and the rotational stiffnesses, k_x, k_y and k_z, are computed while the CHF is deflected γ degrees. The deflection angle γ is limited to $-20° \leq \gamma \leq 20°$. The theory from section 2 is used to compute the occurring stresses during deflections. For optimization, only the support stiffnesses c_x, c_z, and k_y, and the stress distribution are used, which are written as

$$\begin{gathered} k_y^{chf}\left(\gamma, \boldsymbol{p}\right), \quad c_x^{chf}\left(\gamma, \boldsymbol{p}\right), \quad c_z^{chf}\left(\gamma, \boldsymbol{p}\right) \quad \text{with} \quad \boldsymbol{p} = \left[t, d, \boldsymbol{p}_1, \boldsymbol{p}_2, \theta\right], \\ \text{and} \quad \sigma_{eq}^{chf}\left(\boldsymbol{\xi}, \gamma, \boldsymbol{p}\right) \quad \text{with} \quad \boldsymbol{\xi} = \left[\xi_x, \xi_y, \xi_z\right], \end{gathered} \tag{34}$$

to express their dependency on the parameter vector $\boldsymbol{p}$ and σ_{eq}^{chf} is the equivalent von Mises stress defined by equation (33).

3.2 Optimization

The CHF typically has a low actuation stiffness, k_z, and high support stiffnesses c_x, c_z, and k_y [1]. The same is true for an undeflected leaf-spring. However, by choosing the parameters from figure 4(a) correctly, the CHF should be able to retain its support stiffnesses over a wide angle of rotation without exceeding the maximal allowable stress. To achieve this goal, suitable optimization criteria are derived.

3.2.1 Optimization criteria

The performance of the CHF is measured by comparing the support stiffnesses to that of a leaf-spring flexure. To make a fair comparison, the height, length and initial actuation stiffness k_z, determined by the thickness, are equal to the CHF. As a consequence, the model of the leaf-spring flexure is indirectly dependent on the parameter vector $\boldsymbol{p}$, because the actuation stiffness of the CHF is dependent on $\boldsymbol{p}$. By determining at what angle of deflection the support stiffness in a certain direction of the leaf-spring, is equal to the minimum occurring support stiffness of the CHF in that same direction, it can be determined at what angle of deflection the CHF starts to outperform the leaf-spring, see figure 5. For optimal results, this angle should be as close to zero as possible for all support stiffness directions. The support stiffnesses of the leaf-spring flexure, as a function of the deflection angle γ, are written as

$$k_y^{ls}\left(\gamma, \boldsymbol{p}\right), \quad c_x^{ls}\left(\gamma, \boldsymbol{p}\right), \quad c_z^{ls}\left(\gamma, \boldsymbol{p}\right). \tag{35}$$

These stiffnesses decrease monotonically with increasing angle γ, from which it is possible to uniquely determine at which angle γ the support stiffnesses of the leaf-spring are equal to the minimum support stiffnesses of the CHF, resulting in

$$\begin{aligned} k_y^{ls}\left(\gamma_{k_y}(\boldsymbol{p}), \boldsymbol{p}\right) &= \min_{\gamma} k_y^{chf}\left(\gamma, \boldsymbol{p}\right) \quad \rightarrow \quad \gamma_{k_y}(\boldsymbol{p}), \\ c_x^{ls}\left(\gamma_{c_x}(\boldsymbol{p}), \boldsymbol{p}\right) &= \min_{\gamma} c_x^{chf}\left(\gamma, \boldsymbol{p}\right) \quad \rightarrow \quad \gamma_{c_x}(\boldsymbol{p}), \\ c_z^{ls}\left(\gamma_{c_z}(\boldsymbol{p}), \boldsymbol{p}\right) &= \min_{\gamma} c_z^{chf}\left(\gamma, \boldsymbol{p}\right) \quad \rightarrow \quad \gamma_{c_z}(\boldsymbol{p}). \end{aligned} \tag{36}$$

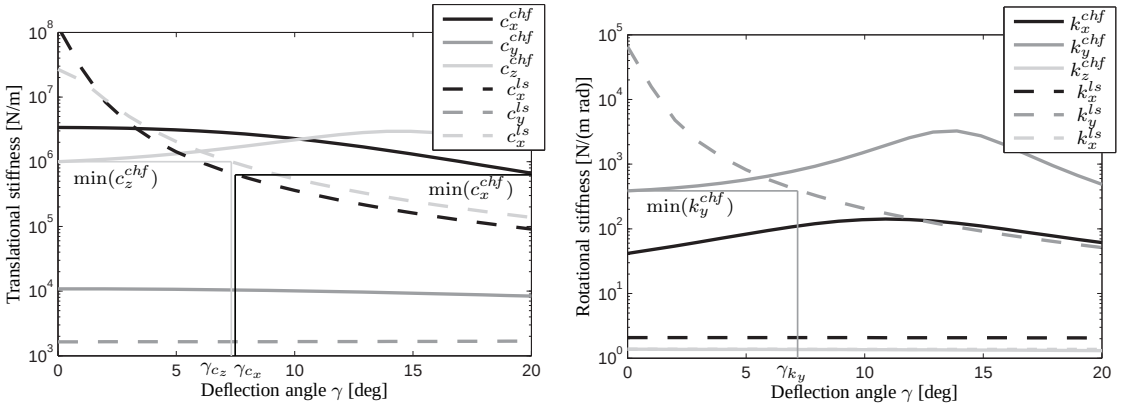

(a) Translational stiffnesses (b) Rotational stiffnesses

Figure 5. Stiffness optimization results, corresponding to the unconstrained parameter optimization. The dotted line represents the leaf-spring stiffnesses and the solid line the CHF stiffnesses.

For optimal results, the maximal value of the angles from equation (36), need to be minimized, resulting in the following minimization criterion and cost function γ_{cost},

$$\boldsymbol{p}_{opt} = \arg\min_{\boldsymbol{p}} \gamma_{cost}(\boldsymbol{p}), \quad \text{with} \quad \gamma_{cost}(\boldsymbol{p}) = \max\left\{\gamma_{k_y}(\boldsymbol{p}), \gamma_{c_x}(\boldsymbol{p}), \gamma_{c_z}(\boldsymbol{p})\right\}, \tag{37}$$

subject to the constraint on the maximal occurring stresses

$$\sigma_{max}^{chf}(\boldsymbol{p}) - \sigma_a \leq 0, \quad \text{with} \quad \sigma_{max}^{chf}(\boldsymbol{p}) = \max_{\boldsymbol{\xi},\gamma}\left(\boldsymbol{\sigma}_{eq}^{chf}\left(\boldsymbol{\xi}, \gamma, \boldsymbol{p}\right)\right), \tag{38}$$

where σ_a is the maximal allowable stress. Constraints on the parameter vector $\boldsymbol{p}$ from equation (34), can be applied to restrict e.g. the minimum thickness t or the distance d between the leaf-springs.

3.2.2 Optimization results

For the optimization, steel X40Cr13 (Stavax) is used as material for the CHF. It is capable of withstanding high stress levels and the maximal allowable stress is therefore set to 600 MPa. The optimization problem

of equations (37) and (38), can be solved using any optimization algorithm which is capable of integrating a non-linear constraint function in the optimization criteria, such as simulated annealing and the Nelder-Mead simplex method. The results of such an optimization are summarized in table 1, where the model is evaluated using the SPACAR software. Two cases are considered: no constraints are applied on the parameter vector and the distance d is constraint to be positive. If the distance d becomes negative for the first case, a different model will be analyzed which places the leaf-springs above each other to avoid that they will physically cross, see figure 6(a). The total height of this CHF model is still the same as the model from figure 4, halving the height of the individual leaf-springs.

	t [mm]	d [mm]	$\boldsymbol{p}_1$ [mm]	$\boldsymbol{p}_2$ [mm]	θ [deg]	σ_a [MPa]	σ_{max}^{chf} [MPa]	γ_{cost} [deg]
unconstraint $\boldsymbol{p}$	0.30	-4.4	[18.2, 1.56]	[38.3, 2.46]	17.4	600	596	7.4
constraint $\boldsymbol{p}$, $d > 0.4$	0.26	0.4	[24.5, 2.10]	[38.3, 2.50]	9.8	600	599	13.5

Table 1. Optimization results summary.

For the unconstrained parameters case, the optimal support stiffnesses are shown in figure 5. It is clear that for deflection angles greater than $7.4°$, the CHF outperforms the leaf-spring flexure and it retains its support stiffnesses over the full range of γ. For the constraint case, it only starts to perform better at an deflection angle of $13.5°$, even though the height of the individual leaf-springs are twice as large compared to the model with negative distance d. This indicates that a more complex CHF with negative distance d, is worth investigating further from a manufacturing point of view.

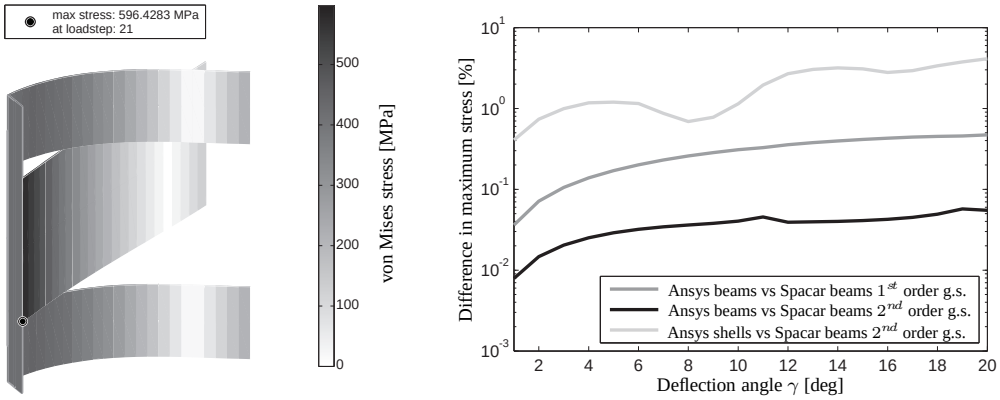

(a) (b)

Figure 6. Computed stress distribution for optimized unconstrained parameter vector model (a). Percentile differences of maximum computed stresses, of the model with and without the second order generalized strain expressions, compared to FEM beam and shell models (b).

3.3 Comparison with FEM

To verify the quality of the stress computation, the maximal computed von Mises stress as a function of the deflection angle, is compared with results from the FEM software Ansys. The optimized CHF model corresponding to the case with the unconstrained parameter vector, shown in figure 6(a), is used as a benchmark. The stress computation is performed using the second order generalized strain expressions of equation (8), and compared to an Ansys model with 60 beam elements (beam4) and a model with 10200 shell elements (shell281). To show the effects of the second order generalized strain expressions on the stresses, they are also computed without the second order generalized strain expressions. The results are shown in figure 6(b), where the percentile errors are computed with respect to the maximal occurring stress of 596 MPa. Using the second order generalized strain expressions, the differences with the Ansys beam element model is an order of magnitude smaller than without the second order generalized strain expressions, although for both cases the error remains small. There is also not much difference in computational time between the Ansys beam and SPACAR models, which is in the order of seconds on a 2.53 GHz processor. However, the stress computation derived in this paper also includes stresses caused by shear forces and torsion, making it more

generally applicable. The effects of shear stresses are in this case very small, because the CHF is only loaded by a bending moment.
The maximum stress computed with the Ansys shell elements, is about 4% higher at 20° deflection. This is most likely due to the phenomenon known as anticlastic curvature, which is the warping of the cross-section of a leaf-spring undergoing a large deflection. This warping is constrained at the end-points when the CHF is modelled with shell elements, increasing the stresses slightly. The computational time is about 8 minutes, making the model with shell elements unsuitable for optimization purposes.

4 CONCLUSIONS

Determining the distributed stress resultants along the elastic line in the local coordinate system, requires correct interpolation and rotation of the vector of element nodal forces. For arbitrary large deflections, perfect equilibrium is achieved in the nodal coordinates of the beam element, making it possible to compute the von Mises stresses at the element cross-section. For improved accuracy, the second order generalized strains should be employed. When compared with a non-linear FEM model with 10200 shell elements, the maximal error in the maximum stress is about 4% due to the anticlastic curvature phenomenon.
The approach is applied to optimize the curved hinge flexure, for high support stiffnesses, low actuation stiffness and with a constraint on the maximal allowable stress. Two optimizations are performed. One where the parameter vector is constraint to prevent physical crossing of the flexures and one where the parameter vector is left unconstrained. In the unconstrained case, physical crossing of the flexures is prevented by placing them above each other. The unconstrained case clearly shows better performance, beating a leaf-spring flexure at 7.4° deflection in terms of support stiffness, versus 13.5° for the constrained case. This indicates that the CHF with its flexures placed above each other, is worth investigating further from a manufacturing point of view.

5 ACKNOWLEDGEMENTS

The authors acknowledge the contributions from Jaap Meijaard in deriving the correct Jacobian matrices.

REFERENCES

[1] BROUWER, D. M., MEIJAARD, J. P., AND JONKER, J. B. Elastic element showing low stiffness loss at large deflection. In *Proceedings of the 24th ASPE Annual Meeting* (Monterey, California, USA, October 4 – 9, 2009).

[2] GÉRADIN, M., AND CARDONA, A. *Flexible multibody dynamics: A finite element approach*, 1st ed. John Wiley and Sons Ltd, Chichester, 2001.

[3] HARINGX, J. The cross-spring pivot as a constructional element. *Applied Scientific Research 1*, 1 (1949), 313–332.

[4] JONKER, J. B., AND MEIJAARD, J. P. Spacar – computer program for dynamic analysis of flexible spatial mechanisms and manipulators. In *Multibody Systems Handbook* (W. Schiehlen (ed.), 123-143, Springer-Verlag, Berlin, 1990).

[5] JONKER, J. B., AND MEIJAARD, J. P. Definition of deformation parameters for the beam element and their use in flexible multibody system analysis. In *ECCOMAS Thematic Conference Multibody Dynamics 2009* (Warsaw University of Technology, June 29 – July 2, 2008).

[6] MEIJAARD, J. P. Validation of flexible beam elements in dynamics programs. *Nonlinear Dynamics 9*, 1-2 (1996), 21–36.

[7] MEIJAARD, J. P., BROUWER, D. M., AND JONKER, J. B. Analytical and experimental investigation of a parallel leaf spring guidance. *Multibody System Dynamics 23*, 1 (2010), 77–79.

[8] TIMOSHENKO, S. P., AND GOODIER, J. N. *Theory of Elasticity*, 3rd ed. McGraw-Hill Book Company, New York, 1951.